Effect of Synthesis Temperature on Transient Photoconductivity of g-C_3N_4 from Urea

Matt D. Capobianco[1,2], Josephine A. Jayworth[1], Bo Shang[1], Nia J. Harmon[1], Hailiang Wang[1,*], and Gary W. Brudvig[1,*]

[1]Department of Chemistry and Yale Energy Sciences Institute, Yale University, New Haven, Connecticut 06520-8107, United States

[2]Department of Chemistry and Biochemistry, California State Polytechnic University, Pomona, California 91768, United States

AUTHOR INFORMATION

Corresponding Authors

gary.brudvig@yale.edu

hailiang.wang@yale.edu

Abstract

Graphitic carbon nitride (g-C_3N_4) is a material that has been at the forefront of heterogenous photocatalysis. Many factors, such as synthesis temperature, have a drastic effect on the photocatalytic ability of g-C_3N_4. In this study, we utilize terahertz (THz) spectroscopy, an ultrafast probe of transient photoconductivity, to understand the effect synthesis temperature has on the photoconductivity of g-C_3N_4. Samples were synthesized at seven different temperatures traditionally used to prepare g-C_3N_4. X-ray diffraction shows that the number of layers increases with increasing synthesis temperature. IR spectroscopy shows that as the synthesis temperature increases, the structure begins to resemble the idealized g-C_3N_4 structure. Optical characterization shows that synthesis temperatures above 600 ºC begin to disrupt the structure. THz photoconductivity is the largest for the sample synthesized at 600 ºC which is corroborated with the greatest photocatalytic CO_2 reduction. This study shows the power THz spectroscopy has in understanding fundamental properties in these emerging materials for photocatalysis.

Introduction

Graphitic carbon nitride (g-C_3N_4), a 2D material, has gained much interest due to its composition of earth abundant elements, robustness, and numerous applications.[1–3] The structure of g-C_3N_4 consists of repeating aromatic carbon-nitrogen six-member rings, but there are many different orientations the carbon and nitrogen atoms can take and the structure will depend greatly on the synthetic conditions used to obtain the sample.[3–7] Some applications of g-C_3N_4 aide in fighting the energy crisis, such as photocatalysis, specifically the hydrogen evolution reaction (HER) and carbon dioxide reduction reaction (CO_2RR).[1,8–13] These photocatalytic rates are drastically affected by synthetic conditions, such as altering the precursors used, annealing temperature, and heating ramp rate.[1,7,14–16] These differences can be directly attributed to the structure of g-C_3N_4 within the photocatalyst.[17] Due to its recent discovery, there is still much to understand about the structure of g-C_3N_4, and ultimately the effect these structural differences have on the photocatalytic rates.

The idealized structure of g-C_3N_4 is a repeating heptazine-based structure which is depicted in Fig. 1a.[1,17] In reality, the actual material is not an idealized structure but rather numerous polymeric carbon nitride polymorphs exist within a bulk g-C_3N_4 sample, and it is difficult to identify which of them construct the sample.[3,5,17] A key difference among the polymorphs is that some contain a 2D repeating structure, like in Fig. 1a, while other contain melon chains that interact using hydrogen bonding (Fig. 1b).[5,17] Work out of the Jacob lab determined that a computationally accurate model of g-C_3N_4 must include small clumps of the idealized structure within a network of melon chains by comparing the computationally determined band gap to the experimentally measured one.[17] Zhang et al. showed that dissolving a sample of g-C_3N_4 in concentrated sulfuric acid can give insight into the structure since melon chains will yield a clear

yellow solution but the idealized structure will give an opaque paste.[9] While there has been much progress made in understanding the structure of g-C_3N_4, there are still ambiguity about the correlation of physical and photocatalytic properties with the structure.

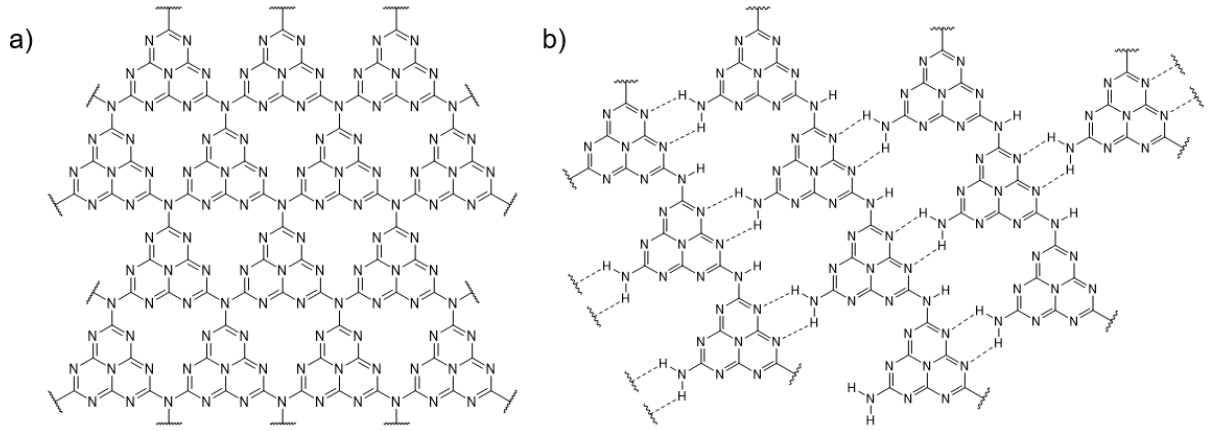

Figure 1. (a) Idealized structure of g-C_3N_4 and (b) structure of melon chains connected via hydrogen-bonding interactions that are denoted by dashed lines.

The differences in structure arise in synthesizing g-C_3N_4, and the conditions utilized can lead to a wide variety of properties in g-C_3N_4.[2,7,14,18–20] Some of the different parameters that are commonly varied include synthetic precursor (urea, thiourea, melamine dicyandiamide, etc.), synthesis temperature (500-650 °C), and temperature ramp-rate.[2,14,18–24] With regards to precursor, there are many nitrogen-rich hydrocarbons, some listed above, but commonly samples synthesized from urea tend to yield the best photocatalysts.[20–22,25] The ideal synthesis temperature depends on the precursor used, but for g-C_3N_4 samples derived from urea, the best photocatalysts are annealed at 600 °C.[19,26] Ultimately, by varying these parameters, the amount of polymerization varies leading to different polymorphs in the material.[3,17] These different polymorphs are what lead to different properties within the material which then affect the photocatalytic rate of the material.[3]

As factors influencing the photocatalytic rate of the g-C_3N_4 continue to be studied, conductivity is critical to probe as it directly relates to the rate of heterogenous catalysis. While studies have alluded to an increase in conductivity when observing an increased HER catalytic rate, there has not yet been a study to quantify the difference in conductive electrons.[9] Terahertz (THz) spectroscopy is a superb technique to study these materials due to it being a non-contact probe of conductive electron with sub-picosecond time resolution.[27–29] As opposed to other techniques to measure conductivity that require physical contacts and examine the bulk conductivity, THz spectroscopy probes conductivity within the material without the need for physical contacts, which is necessary for nanomaterials.[27–29] By pairing a THz probe beam with a visible pump, time-resolved photoconductivity of the material can be measured, which provides lifetimes for the excited electrons responsible for photocatalysis.[28–30] THz spectroscopy has been utilized for many photocatalytic materials, such as transition metal dichalcogenides, MOFs, graphene, and many more, to corroborate photoconductivity and photocatalysis.[29,31–35] There have been time-resolved photoluminescence studies done on g-C_3N_4 which didn't show a significant dependence on the synthesis temperature.[36–38] To the best of our knowledge, g-C_3N_4 from urea synthesized at different temperatures has yet to be studied with time-resolved THz spectroscopy.

Herein, we utilize THz spectroscopy to measure the transient photoconductivity of g-C_3N_4 synthesized from urea at different temperatures. The materials are characterized to understand how the physical and electronic properties are affected by the synthesis temperature. The transient photoconductivity was then measured for each sample synthesized at the different temperatures and then correlated with photocatalytic measurements. It was found that samples synthesized at 600 ºC had the highest THz photoconductivity signal which agrees with previous photocatalytic studies as well as the CO_2 photoreduction measurements done here. The enhanced

photoconductivity can be attributed to more of the idealized structure arising from the higher synthesis temperature. Temperatures above 600 ºC begin to disrupt the structure leading to a reduction of the photoconductivity and photocatalysis. Overall, this study paves the way for understanding how structural changes in g-C_3N_4 affect the photoconductivity and photocatalytic properties of the material.

Materials and Methods

Synthesis of g-C_3N_4 from Urea

To prepare the samples, about 20 g of urea (Sigma-Aldrich, ≥ 98% purity) was measured and placed into an alumina crucible with aluminum foil around the top. The crucible was placed into a muffle furnace where it was kept at its respective temperature for two hours with a ramp rate of 300 ºC/hr. The samples were allowed to ambiently cool back to room temperature and were then removed, massed, and placed into a vial. Samples will be denoted by U, because of the urea precursor, followed by their synthesis temperature; thus, the sample synthesized at 500 ºC will be referred to at U500. The resulting materials are shown in Fig. S1.

In addition to these powder samples, films were created by making a 5 g mixture of 15 % by weight polyvinyl butyral (PVB) in ethanol. Once the PVB was fully dissolved, about 100 mg of sample was added to the mixture, then stirred until there were no observable pieces of material. The paste was then doctor-bladed onto a piece of quartz cleaned by sonicating in DI water, acetone, isopropanol, and ethanol separately for about 20 minutes. Doctor-blading was conducted by placing scotch tape as a spacer, placing some of the paste onto the top piece of tape, and then coated using a pasture pipet. Samples were air-dried to ensure the ethanol was evaporated off. Samples used for THz measurements required 5 layers, which was done by first depositing one

layer, letting the sample air-dry, then putting a 2nd layer of tape to doctor-blade, and then continuing up to 5 layers.

Materials Characterization

X-ray diffraction (XRD) measurements were done on the powder samples using a Rigaku SmartLab XRD which includes a Cu Kα source with a beam energy of 8.04 keV, corresponding to an x-ray wavelength of 1.5406 Å. The surface area was determined by the BET method using a Micromeritics ASAP 2460 surface area and porosity analyzer with nitrogen adsorption isotherms collected at 77 K. When samples were dissolved in concentrated sulfuric acid, 100 mg of sample were dissolved in 1 mL of acid, and then stirred at 100 °C.[9] Elemental analysis was done through Robertson-Microlit labs. Inductively coupled plasma mass spectrometry (ICP-MS) measurements were obtained using a NexION 5000 Multi-Quadrupole ICP mass spectrometer. Fourier transformed infrared (FTIR) spectroscopy was performed using an Agilent Cary 660 instrument. UV-Vis diffuse reflectance measurements were done using a Shimadzu UV-2600 with an integrating sphere attachment. The Kubelka-Munk transformation (F(R)), shown below, was applied to the reflectance (R) data.

$$\mathrm{F(R)} = \frac{(1-\mathrm{R})^2}{2\mathrm{R}} \qquad [equation\ 1]$$

Photoluminescence measurements were collected using a Horiba Fluoromax Plus spectrometer. Film thicknesses were measured using a Dektak mechanical profilometer.

Terahertz Spectroscopy

The spectrometer setup is described in detail in our previous publications.[29,32,33] For an optical-pump terahertz-probe (OPTP) measurement, the terahertz pulse transmitted through a

sample was measured. Then, the probe delay stage was set to the maximum amplitude of the pulse, and an OPTP trace was collected by monitoring the change in that peak amplitude versus the pump delay time. The raw OPTP trace is transformed into %ΔTHz by dividing the raw data by the value of the peak of the THz time-domain pulse. All measurements were done with 400 nm excitation pulses at a power of 100 mW. For time-resolved terahertz spectroscopy (TRTS) measurements, the pump delay stage was fixed to 1 ps after excitation and the photoexcited THz pulse was measured. In addition to the photoexcited pulse, a non-photoexcited pulse was also collected. The complex-valued conductivity was extracted using the Nelly program previously developed by our lab.[39]

Photocatalytic CO_2 Reduction Measurements

Cobalt phthalocyanine-tetracarboxylic acid (CoPc-COOH) molecules were first synthesized using a reported method.[40] g-C_3N_4 synthesized at different temperatures was then functionalized with CoPc-COOH. This was done by first dispersing 30 mg of g-C_3N_4 in 30 mL of dimethylformamide (DMF), and sonication was used to ensure all particles were fully dispersed. Once the sample was fully dispersed, 5% by weight of CoPc-COOH was placed into the g-C_3N_4 dispersion and then sonicated for an hour followed by vigorously stirring for 24 hours. After stirring, the sample was centrifuged for 15 minutes at 1200 rpm followed by decanting the supernatant, and washing with DMF then water. Samples were then freeze dried and then the obtained powder was stored in air for further tests.

Photocatalytic measurements were carried out by measuring out 3 mg of the carbon nitride decorated with CoPc-COOH and suspending it in 5 mL of a 3:1 mixture by volume of acetonitrile and triethanolamine. Sonication was utilized if the material was not fully dispersed. The vial was purged with CO_2 for about 10 minutes. The sample was then illuminated using a 150 W Xe lamp

(ABET technologies) with a AM1.5G light filter and a light intensity of approximately 300 mW/cm^2. The concentration of the generated CO and H_2 was quantified using an online gas-chromatograph (SRI GC) every 10 mins during the photocatalysis.

Results and Discussion

To examine the effect that synthesis temperature has on the structure, XRD and IR spectroscopy were utilized. The XRD patterns for each temperature are displayed in Fig. 2, where the major (002) peak around 27° corresponds to the inter-sheet stacking and the less intense (100) peak around 13° corresponds to the intra-sheet pattern of the material.[5,21,32] Focusing on the inter-sheet stacking peak, there is an observable shift to higher 2θ and a sharpening of the feature with increasing synthesis temperature. The sharpening of this feature, with regards to increasing temperature, implies the creation of more ordered domains within the g-C_3N_4 structure. The shift to a higher 2θ for the (002) peak indicates a decrease in the inter-layer distance of the structure which can be quantified by fitting the peak with a Lorentzian, then modeling with the Bragg equation (eq. 2). In the Bragg equation, λ is the wavelength of the x-rays, θ is the angle the x-ray hits the sample, and d is the interlayer distance. The calculated inter-layer distances are displayed in Table 1 showing a decrease from 3.28 Å to 3.21 Å for U500 to U650. The shift to higher 2θ also suggests a transition from triazine to heptazine subunits.[5] An estimate of particle size can be gained from the same Lorentzian fit, except now modeling with the Scherrer equation (eq. 3). In the Scherrer equation, λ and θ are the same as in the Bragg equation, β is the FWHM, and D is the grain size. Using the information gained from the Bragg's law and the Scherrer equation, an estimate for the number of layers is obtained and displayed in Table 1. An increase in the number of layers is observed as the synthesis temperature is increased, implying there is more order within

the sample and better stacked particles. BET measurements displayed in Table 1 show that the surface area increases until U600 which is consistent with a previous report.[18]

$$\lambda = 2d \sin\theta \qquad [equation\ 2]$$

$$D = \frac{\lambda}{\beta \cos\theta} \qquad [equation\ 3]$$

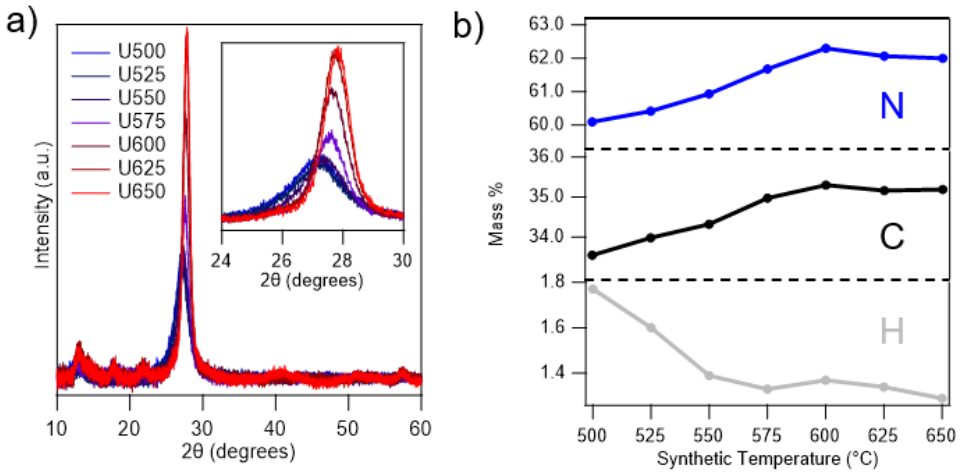

Figure 2. (a) powder XRD for each sample; inset: (002) diffraction peak showing the inter-layer distance. (b) elemental analysis for nitrogen (blue), carbon (black) and hydrogen (gray) as a function of synthesis temperature.

Further understanding is obtained about the structure, with regards to the polymerization, by dissolving the samples in concentrated sulfuric acid.[9] Fig. S2 displays the resulting solutions after heating and mixing in acid. U500 and U525 resulted in a yellow solution suggesting these materials consisted of more H-bonding and melon chains than other samples. Then, solutions trended toward more opaque and thicker samples up to U600 suggesting they contain more of the idealized structure and less H-bonding. Solutions of U625 and U650 are still opaque but are less

viscous than U600 suggesting at those temperatures more defects are created. Elemental analysis is performed to understand the composition of the material synthesized at different materials. The amounts of carbon and nitrogen increase and the amount of hydrogen decreases with synthesis temperature until U600, and then level off. This is consistent with the acid dissolving experiment showing that there are less melon chains, and therefore less terminal amine protons, at the higher synthesis temperatures. The carbon to nitrogen ratio, displayed in Fig. S3, is around 0.66 which is consistent with previous reports.[14,32,41] There is a slight increase in the C:N ratio with an increase in synthesis temperature which suggests more of the idealized structure.

Table 1. Stacking Properties and Surface Area

	Interlayer Distance (Å)	**Approximate number of layers**	**BET Surface Area (m^2/g)**
U500	3.28	13	33.83
U525	3.28	14	44.65
U550	3.26	17	62.08
U575	3.24	24	84.51
U600	3.22	27	93.51
U625	3.21	29	88.15
U650	3.21	31	65.02

More information on the effect the synthesis temperature has on the structure, specifically the chemical bonding of g-C_3N_4, is gained through IR spectroscopy. The IR spectra for samples prepared at the various synthesis temperatures are displayed in Fig. 3 and are normalized to the

resonance at 1631 cm^{-1} which corresponds to C=N or C=C stretches. The peaks around 1315 cm^{-1}, 1230 cm^{-1}, and 1200 cm^{-1} (Fig. 3 red panel) correspond to tertiary amines.[14,42] As the synthesis temperature is increased, these features begin to grow, as well as becoming sharper, meaning there are more tertiary amines. This would suggest that as the synthesis temperature increases, there is more of the idealized g-C_3N_4 structure; this is consistent with the elemental analysis. As the synthesis temperature is increased, a doublet forms around 1580 cm^{-1} (Fig. 3 blue panel) which corresponds to heptazine units, suggesting that at lower synthesis temperatures some of the material may be triazine.[14,42] This is consistent with the XRD trend. The feature seen around 810 cm^{-1} (Fig. 3 green panel) corresponds to both triazine and heptazine units which confirms that a carbon-nitrogen structure has been formed.[14,42] There is not a significant dependence on synthesis temperature for this feature again showing there is a carbon-nitride material at all synthetic temperatures. The set of features centered at 3200 cm^{-1} (Fig. 3 orange panel) corresponds to N-H stretches.[14,42] The peaks in this region generally increased with synthesis temperature, peaking at 600 ºC. This is due to there being more of the melon chain structure at lower temperatures, where the N-H protons will exist in hydrogen bonding, and therefore these IR features with either be broadened or attenuated. Then, at higher temperatures, when more of an idealized g-C_3N_4 structure is observed, the peaks centered at 3200 cm^{-1} are sharper because N-H features now exist mostly on the edges and therefore are free to vibrate. This theory is consistent with the elemental analysis, which shows less hydrogen content as the synthesis temperature is increased. It was determined that the products formed after 2 hours of annealing are the thermodynamic products by comparing the XRD patterns (Fig. S4) and IR spectra (Fig. S5) for samples annealed for different lengths of time at 500 °C and 600 °C.

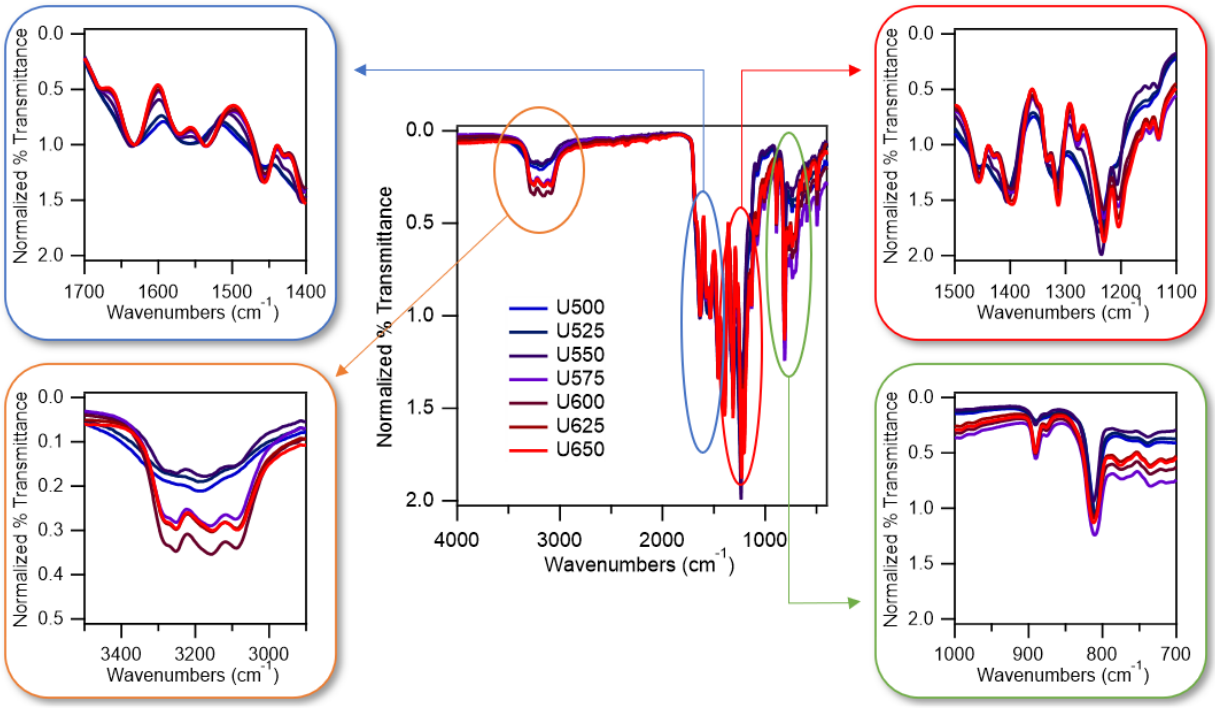

Figure 3. IR spectra for samples prepared at each synthesis temperature with zoomed in regions of interest shown in the side panels.

In addition to structural changes, the optical properties are affected by the synthesis temperature. The Kubelka-Monk UV-Vis diffuse reflectance spectra of the samples from the different synthesis temperatures are shown in Fig. 4 with the excitation wavelength of OPTP measurements denoted by the solid black line. The sample synthesized at 650 ºC shows a shoulder growing at longer wavelength in which is attributed to a n (lone pair) to π^* transition due to distortion in the g-C_3N_4 sheets.[43,44] Further understanding on the electronic structure is obtained through Tauc analysis; the extracted band-gaps are shown in Table 2 (plots are shown in Fig. S6). Most of the synthesis temperatures lead to samples with a band transition around 2.7 eV, which is similar to the reported value for bulk g-C_3N_4.[17,23,32] Starting at 575 ºC, there is another transition

which is shown to be around 2.9 eV. The growth of this band feature can be attributed to more of the idealized structure of g-C_3N_4.[17] Then, for the sample synthesized at 650 ºC, there are three observed features. The extracted band-gap values slightly differ from other samples, and the additional smaller band feature can be attributed to the material that has started to lose the g-C_3N_4 structure at this higher synthesis temperature.

Table 2. Band-gaps from Tauc Analysis.

	Band-gap(s) (eV)
U500	2.72 ± 0.01
U525	2.69 ± 0.01
U550	2.65 ± 0.02
U575	2.70 ± 0.02, 2.84 ± 0.01
U600	2.69 ± 0.03, 2.88 ± 0.03
U625	2.62 ± 0.02, 2.91 ± 0.01
U650	2.16 ± 0.04, 2.50 ± 0.02, 2.92 ± 0.03

Additional information of the electronic structure is acquired using steady-state photoluminescence (PL) measurements; resulting emission spectra of the various g-C_3N_4 samples due to excitation from 350 nm light are displayed in Fig. 4b. The PL peak is around 450 – 500 nm (2.75 – 2.48 eV) for samples prepared at different synthesis temperatures, which is consistent with previous reports of the material.[45–47] Overall, there is a significant red-shift in the peak as the synthesis temperature is increased. This shift is quantified by fitting the data by appropriately transforming the data from wavelength to energy.[48] As suggested by previous reports, three

different components best model the PL peak, and those are shown in Fig. S7.[45,46] The resulting energy positions, and relative areas, are shown in Table S1. The three components are around 2.3 eV, 2.5 eV, and 2.7 eV with small variations for samples prepared at different synthesis temperatures. There is a decrease in the relative area for the 2.7 eV component for samples prepared at the higher synthesis temperature implying an overall red shift in the feature. This is most noticeable for U625 and U650 suggesting that there are more sub-band states for the electrons to occupy in samples prepared at those temperatures, which is due to defect sites from structural deformations.

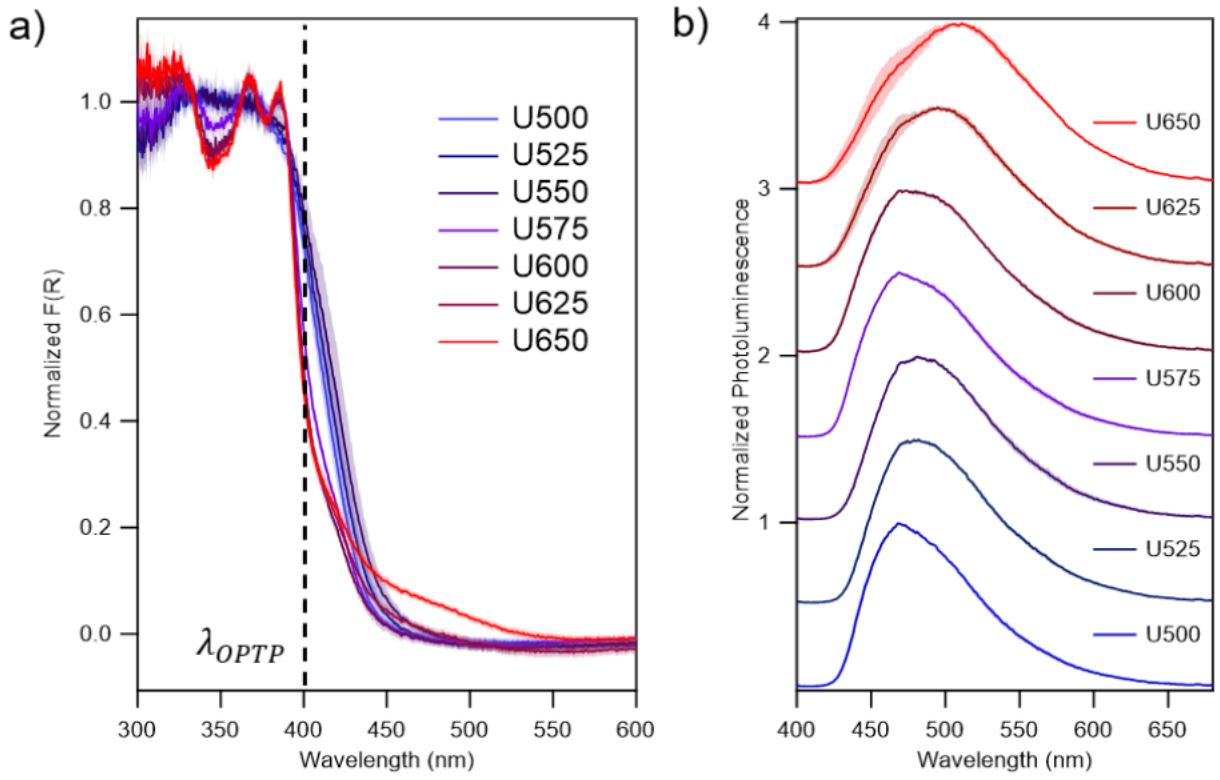

Figure 4. (a) Normalized Kubelka-Munk UV-Vis diffuse reflectance spectra; the excitation wavelength used for OPTP experiments is shown with a dashed line. (b) Normalized

photoluminescence spectra with an excitation wavelength of 350 nm. In both figures, the shaded regions show the standard deviation of 4 samples.

While the effect of synthesis temperature on the structure has been thoroughly studied previously, there has yet to be quantification of the effect it has on photoconductivity. Optical-pump terahertz-probe (OPTP) is superb tool to probe photoconductivity in 2D materials and is utilized on the g-C_3N_4 synthesized at different temperatures. This was done by exciting the g-C_3N_4 samples with 400 nm light, which all absorb at as shown by Fig. 4a, and monitoring how the peak THz signal changes for samples synthesized at different temperatures. For uniformity, the samples were mixed with PVB and deposited onto quartz; the resulting thickness are in Table S2 and the profiles are in Fig. S8. To confirm the PVB is not altering the material, three different sample preparations are done and no significant changes in the OPTP dynamics (Fig. S9) are observed.[49] The OPTP trace for each synthesis temperature is shown averaged over two spots on four samples in Fig. 5a. The corresponding graphs with standard deviation for each of the synthesis temperatures as shaded regions are shown in Fig. S10. The OPTP traces are fit with a single exponential (eq. 4) to learn about the photoexcited carrier properties. In eq. 4, A is the amplitude of the signal, τ is the relaxation lifetime, y_0 is the long-term offset, and G_R(FWHM) is a Gaussian convolution to represent the instrument response function limited by the pulse width of the pump beam.

$$\Delta THz = \left[Ae^{-\frac{t}{\tau}} + y_0\right] \otimes G_R(FWHM) \qquad [equation\ 4]$$

The full fit results are displayed in Table S3 for all samples as well as the average and standard deviation for samples prepared at each synthesis temperatures. Fig. 5b displays the average amplitudes for samples at each temperature, which shows the sample synthesized at 600 °C yields the largest amplitude. The trend that is observed with amplitude relative to synthesis temperature

is consistent with photocatalytic rates that have been previously observed throughout the literature.[19,26] The amplitude versus normalized percent reflectance at 400 nm (Fig. S12) shows that there is an inverse relationship between the properties. This implies that the difference in amplitude is not due to a change in absorption in the material, but rather a change in the structure of the material. The average lifetimes are shown in Fig. S11a, and there is no significant change for samples prepared at the lowest three synthesis temperatures as they are all around 7 ps. Then, for U575, the lifetime decreases to about 3 ps and this is the sample where the second band begins to grow in for the Tauc analysis. Also, for the higher temperatures, with regards to the PL, there is less contribution from the direct band relaxation. The optical characterization suggests that there are more sub-band states, which are usually non-mobile states and therefore will not absorb THz radiation, which could lead to the lower lifetime for the higher synthesis temperatures. This is also the point where an increase in the idealized g-C_3N_4 becomes more predominate in the sample, as suggested by the IR spectroscopy and the acid-dissolving experiments. This trend would explain the observed improved photoconductivity for the sample synthesized at 600 °C, and therefore why it has been reported with the best photocatalytic activity. The long-term offset (y_0) doesn't show a significance difference (Fig. S11b) between samples prepared at different temperatures, which could be due to building blocks of the structure being the same at all temperatures.

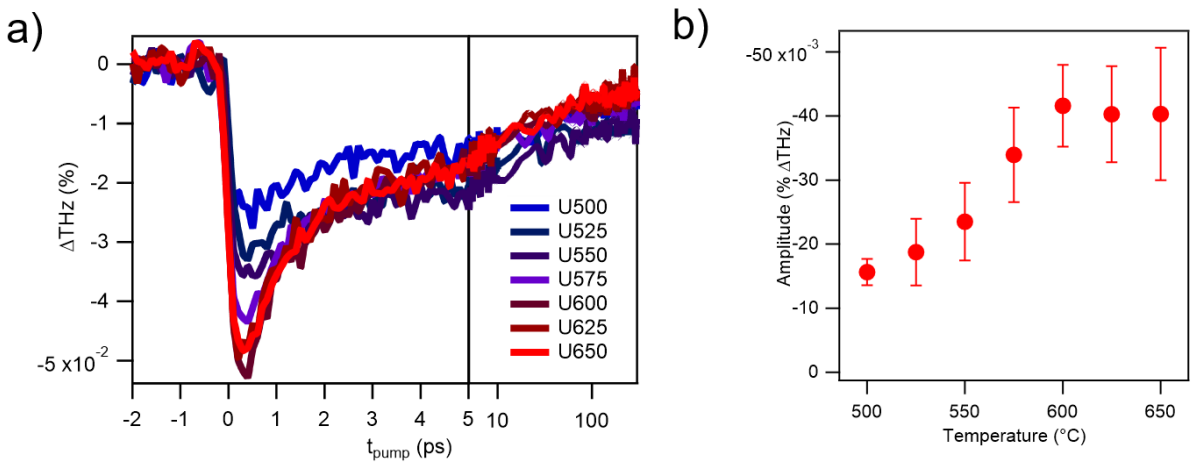

Figure 5. (a) Average OPTP traces of eight measurements for each sample. (b) The average amplitude from a single exponential fit with respective standard deviations.

More understanding of the photoconductivity is achieved through the frequency-dependent time-resolved terahertz spectroscopy (TRTS) technique. This technique measures the entire terahertz pulse, and through a Fourier transform, the complex-valued frequency-dependent photoconductivity is extracted. This technique was done for each of the samples and the resulting photoconductivity data are displayed in Fig. S13. There is not any significant change seen in the spectra for samples prepared throughout the temperatures except there appears to be a phonon resonance growing in at about 1.2 THz for the sample prepared at 575 °C. This is the temperature where many characterizations saw significant changes, but further studies would need to be done to determine the exact origin of this resonance. The Drude-Smith model (eq. 5) provides even more insight into the properties of the photoexcited carriers. In this equation, σ_0 represents the DC photoconductivity, τ_s is the scattering lifetime of the electron, and the c-parameter (c) is the persistence of velocity.[50,51] For the c-parameter, a value of 0 is for larger crystals where electrons relax before reaching the edge of a crystalline domain and a value of 1 is for smaller particles where most carriers will interact with the grain boundary before relaxing.

$$\sigma(\omega) = \frac{\sigma_0}{1 - i\omega\tau_s}\left(1 + \frac{c}{1 - i\omega\tau_s}\right) \qquad [equation\ 5]$$

The fit results are displayed in Table S4 with the results of fitting to the Drude-Smith model being displayed in Fig. S13. These fit results show a decrease in the c-parameter with increasing synthesis temperature which is consistent with the XRD results showing grain sizes increasing. The scattering lifetime increases with increasing temperature which is related to the grain size but also may relate to the increase in amplitude seen in the OPTP data. Overall, there is an increase in photoconductivity which is most likely due to forming more of the idealized g-C_3N_4 structure. But eventually, at the higher synthesis temperatures, defects begin to grow in which introduce more recombination sites.

To corroborate this physical property of photoconductivity with actual catalysis performed, the CO_2RR rate is investigated. To do CO_2 reduction, the samples synthesized at different temperatures are decorated with cobalt phthalocyanine tetracarboxylic acid (CoPc-COOH).[40] The CoPc-COOH photocatalysts load differently which can be seen visually (Fig. S14) and quantitively (Table S5) by ICP-MS. The CoPc-COOH attaches itself through free amino groups, and therefore samples prepared at the lower synthesis temperatures have worse loading because most amino groups are involved in H-bonding. For the U650 samples, the loading begins to worsen again because the high temperature alters the structure. Fig. 6 displays the amount of CO produced from photochemical reduction of CO_2 for each g-C_3N_4 sample. Consistent with the OPTP measurements, the U600 sample yielded the highest photocatalytic rate. For all the temperatures, the photocatalytic rate depends on both the catalyst loading and the photoconductivity. For example, while the U625 and U650 samples had similar OPTP amplitudes, the loading on U650 was much worse, most likely due to disruption to the structure, leading to a decrease in the

photocatalytic rate. Then for the U550 and U575 samples, there was similar catalyst loading but U575 had a larger OPTP amplitude which correlates with the enhance photocatalytic rate. These studies add excellent agreement to photoconductivity studies in this work.

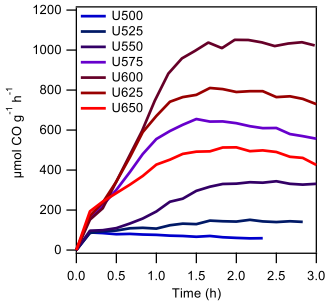

Figure 6. Photocatalytic CO_2 reduction rate to CO for samples decorated with CoPc.

Conclusions

In conclusion, we utilized pump-probe THz spectroscopic techniques to quantify the photoconductivity differences in g-C_3N_4 arising from variations in the structure of the samples prepared at the different synthesis temperatures. To the best of our knowledge, this is the first report of THz photoconductivity in g-C_3N_4 from urea, and the first observation of an appreciable OPTP signal for any g-C_3N_4 sample. To look at the effect of synthesis temperature, seven different temperatures between 500 ºC and 650 ºC were used. The samples were thoroughly characterized

and the observed trends were consistent with previous reports of similar systems. Overall, at the lower synthesis temperature, the materials consist mostly of melon chains. Then around 575 ºC, the polymerization begins to be more complete and create the idealized g-C_3N_4 structure. Eventually, at the higher synthesis temperatures, there begins to be some structural defects. OPTP results show that the U600 sample has the largest photoconductivity which is corroborated with the highest rate of photocatalytic CO_2 reduction. This study provides crucial insight into an important heterogenous material used in many different catalytic fields and paves the way for further photocatalytic enhancement.

ASSOCIATED CONTENT

Supporting Information.

The following files are available free of charge.

Image of synthesized materials; image of materials dissolved in acid; carbon to nitrogen ratio from the elemental analysis; XRD and IR for different synthesis times; Tauc plots with corresponding linear fits; peak fitting for PL; thickness from profilometry; OPTP comparison for different sample preparation; OPTP averages with corresponding single exponential fit; TRTS results with corresponding Drude-Smith fit results; CoPc-COOH loading; Normalized photocatalysis results. This material is available free of charge via the Internet at http://pubs.acs.org.

AUTHOR INFORMATION

Notes

The authors declare no competing financial interests.

ACKNOWLEDGMENT

This work was supported by the U.S. National Science Foundation (Grant CHE-1954453). Materials characterization work was supported by the U.S. Department of Energy (DOE), Office of Science, Office of Basic Energy Sciences, Chemical Sciences, Geosciences, and Biosciences Division under contract DE-FG02-07ER15909 (J.A.J. and G.W.B.).

References

(1) Wang, X.; Maeda, K.; Thomas, A.; Takanabe, K.; Xin, G.; Carlsson, J. M.; Domen, K.; Antonietti, M. A Metal-Free Polymeric Photocatalyst for Hydrogen Production from Water under Visible Light. *Nat. Mater.* **2009**, *8* (1), 76–80. https://doi.org/10.1038/nmat2317.

(2) Abu-Sari, S. M.; Daud, W. M. A. W.; Patah, M. F. A.; Ang, B. C. A Review on Synthesis, Modification Method, and Challenges of Light-Driven H_2 Evolution Using g-C_3N_4-Based Photocatalyst. *Adv. Colloid Interface Sci.* **2022**, *307*, 102722. https://doi.org/10.1016/j.cis.2022.102722.

(3) Vidyasagar, D.; Bhoyar, T.; Singh, G.; Vinu, A. Recent Progress in Polymorphs of Carbon Nitride: Synthesis, Properties, and Their Applications. *Macromol. Rapid Commun.* **2021**, *42* (7), 2000676. https://doi.org/10.1002/marc.202000676.

(4) Praus, P. A Brief Review of S-Triazine Graphitic Carbon Nitride. *Carbon Lett.* **2022**, *32* (3), 703–712. https://doi.org/10.1007/s42823-022-00319-9.

(5) Fina, F.; Callear, S. K.; Carins, G. M.; Irvine, J. T. S. Structural Investigation of Graphitic Carbon Nitride via XRD and Neutron Diffraction. *Chem. Mater.* **2015**, *27* (7), 2612–2618. https://doi.org/10.1021/acs.chemmater.5b00411.

(6) Liu, N.; Li, T.; Zhao, Z.; Liu, J.; Luo, X.; Yuan, X.; Luo, K.; He, J.; Yu, D.; Zhao, Y. From Triazine to Heptazine: Origin of Graphitic Carbon Nitride as a Photocatalyst. *ACS Omega* **2020**, *5* (21), 12557–12567. https://doi.org/10.1021/acsomega.0c01607.

(7) Miller, T. S.; Jorge, A. B.; Suter, T. M.; Sella, A.; Corà, F.; McMillan, P. F. Carbon Nitrides: Synthesis and Characterization of a New Class of Functional Materials. *Phys.*

Chem. Chem. Phys. **2017**, *19* (24), 15613–15638. https://doi.org/10.1039/C7CP02711G.

(8) Dong, X.; Cheng, F. Recent Development in Exfoliated Two-Dimensional g-C_3N_4 Nanosheets for Photocatalytic Applications. *J. Mater. Chem. A* **2015**, *3* (47), 23642–23652. https://doi.org/10.1039/C5TA07374J.

(9) Zhang, H.; Cao, Y.; Li, Z.; Gao, Y.; Shangguan, L.; Sun, J.; Lang, L.; Lei, W. Improved Charge Transport through 2D Framework in Fully Condensed Carbon Nitride for Efficient Photocatalytic Hydrogen Production. *J. Catal.* **2023**, *417*, 360–367. https://doi.org/10.1016/j.jcat.2022.12.018.

(10) Liu, B.; Xu, B.; Li, S.; Du, J.; Liu, Z.; Zhong, W. Heptazine-Based Porous Graphitic Carbon Nitride: A Visible-Light Driven Photocatalyst for Water Splitting. *J. Mater. Chem. A* **2019**, *7* (36), 20799–20805. https://doi.org/10.1039/C9TA03646F.

(11) Cao, S.; Yu, J. G-C_3N_4-Based Photocatalysts for Hydrogen Generation. *J. Phys. Chem. Lett.* **2014**, *5* (12), 2101–2107. https://doi.org/10.1021/jz500546b.

(12) Su, Q.; Sun, J.; Wang, J.; Yang, Z.; Cheng, W.; Zhang, S. Urea-Derived Graphitic Carbon Nitride as an Efficient Heterogeneous Catalyst for CO_2 Conversion into Cyclic Carbonates. *Catal. Sci. Technol.* **2014**, *4* (6), 1556. https://doi.org/10.1039/c3cy00921a.

(13) Cometto, C.; Kuriki, R.; Chen, L.; Maeda, K.; Lau, T.-C.; Ishitani, O.; Robert, M. A Carbon Nitride/Fe Quaterpyridine Catalytic System for Photostimulated CO_2 -to-CO Conversion with Visible Light. *J. Am. Chem. Soc.* **2018**, *140* (24), 7437–7440. https://doi.org/10.1021/jacs.8b04007.

(14) Alwin, E.; Kočí, K.; Wojcieszak, R.; Zieliński, M.; Edelmannová, M.; Pietrowski, M. Influence of High Temperature Synthesis on the Structure of Graphitic Carbon Nitride

and Its Hydrogen Generation Ability. *Materials* **2020**, *13* (12), 2756. https://doi.org/10.3390/ma13122756.

(15) Paul, D. R.; Sharma, R.; Nehra, S. P.; Sharma, A. Effect of Calcination Temperature, PH and Catalyst Loading on Photodegradation Efficiency of Urea Derived Graphitic Carbon Nitride towards Methylene Blue Dye Solution. *RSC Adv.* **2019**, *9* (27), 15381–15391. https://doi.org/10.1039/C9RA02201E.

(16) Yang, W.; Jia, L.; Wu, P.; Zhai, H.; He, J.; Liu, C.; Jiang, W. Effect of Thermal Program on Structure–Activity Relationship of g-C_3N_4 Prepared by Urea Pyrolysis and Its Application for Controllable Production of g-C_3N_4. *J. Solid State Chem.* **2021**, *304*, 122545. https://doi.org/10.1016/j.jssc.2021.122545.

(17) Im, C.; Kirchhoff, B.; Krivtsov, I.; Mitoraj, D.; Beranek, R.; Jacob, T. Structure and Optical Properties of Polymeric Carbon Nitrides from Atomistic Simulations. *Chem. Mater.* **2023**, *35* (4), 1547–1559. https://doi.org/10.1021/acs.chemmater.2c02843.

(18) Fang, H.-B.; Luo, Y.; Zheng, Y.-Z.; Ma, W.; Tao, X. Facile Large-Scale Synthesis of Urea-Derived Porous Graphitic Carbon Nitride with Extraordinary Visible-Light Spectrum Photodegradation. *Ind. Eng. Chem. Res.* **2016**, *55* (16), 4506–4514. https://doi.org/10.1021/acs.iecr.6b00041.

(19) Dong, F.; Wu, L.; Sun, Y.; Fu, M.; Wu, Z.; Lee, S. C. Efficient Synthesis of Polymeric G-C_3N_4 Layered Materials as Novel Efficient Visible Light Driven Photocatalysts. *J. Mater. Chem.* **2011**, *21* (39), 15171–15174. https://doi.org/10.1039/C1JM12844B.

(20) Zhang, W.; Zhang, Q.; Dong, F.; Zhao, Z. The Multiple Effects of Precursors on the Properties of Polymeric Carbon Nitride. *Int. J. Photoenergy* **2013,** *10*, 658083. http://dx.doi.org/10.1155/2013/685038.

(21) Ismael, M.; Wu, Y.; Taffa, D. H.; Bottke, P.; Wark, M. Graphitic Carbon Nitride Synthesized by Simple Pyrolysis: Role of Precursor in Photocatalytic Hydrogen Production. *New J. Chem.* **2019**, *43* (18), 6909–6920. https://doi.org/10.1039/C9NJ00859D.

(22) Devthade, V.; Kulhari, D.; Umare, S. S. Role of Precursors on Photocatalytic Behavior of Graphitic Carbon Nitride. *Mater. Today Proc.* **2018**, *5* (3, Part 1), 9203–9210. https://doi.org/10.1016/j.matpr.2017.10.045.

(23) Nguyen, T. K. A.; Pham, T.-T.; Nguyen-Phu, H.; Shin, E. W. The Effect of Graphitic Carbon Nitride Precursors on the Photocatalytic Dye Degradation of Water-Dispersible Graphitic Carbon Nitride Photocatalysts. *Appl. Surf. Sci.* **2021**, *537*, 148027. https://doi.org/10.1016/j.apsusc.2020.148027.

(24) Li, X.; Melissen, S. T. A. G.; Le Bahers, T.; Sautet, P.; Masters, A. F.; Steinmann, S. N.; Maschmeyer, T. Shining Light on Carbon Nitrides: Leveraging Temperature To Understand Optical Gap Variations. *Chem. Mater.* **2018**, *30* (13), 4253–4262. https://doi.org/10.1021/acs.chemmater.8b00740.

(25) Gao, Y.; Duan, J.; Zhai, X.; Guan, F.; Wang, X.; Zhang, J.; Hou, B. Extraordinary Photodegradation Performance of Graphitic Carbon Nitride Derived from Tin Foil–Wrapped Urea. *J. Nanoparticle Res.* **2021**, *23* (2), 44. https://doi.org/10.1007/s11051-020-05111-2.

(26) Wang, Z.-T.; Xu, J.-L.; Zhou, H.; Zhang, X. Facile Synthesis of Zn(II)-Doped g-C_3N_4 and Their Enhanced Photocatalytic Activity under Visible Light Irradiation. *Rare Met.* **2019**, *38* (5), 459–467. https://doi.org/10.1007/s12598-019-01222-5.

(27) Neu, J.; Schmuttenmaer, C. A. Tutorial: An Introduction to Terahertz Time Domain Spectroscopy (THz-TDS). *J. Appl. Phys.* **2018**, *124* (23), 231101. https://doi.org/10.1063/1.5047659.

(28) Han, P.; Wang, X.; Zhang, Y. Time-Resolved Terahertz Spectroscopy Studies on 2D Van Der Waals Materials. *Adv. Opt. Mater.* **2020**, *8* (3), 1900533. https://doi.org/10.1002/adom.201900533.

(29) Spies, J. A.; Neu, J.; Tayvah, U. T.; Capobianco, M. D.; Pattengale, B.; Ostresh, S.; Schmuttenmaer, C. A. Terahertz Spectroscopy of Emerging Materials. *J. Phys. Chem. C* **2020**, *124* (41), 22335–22346. https://doi.org/10.1021/acs.jpcc.0c06344.

(30) Ulbricht, R.; Hendry, E.; Shan, J.; Heinz, T. F.; Bonn, M. Carrier Dynamics in Semiconductors Studied with Time-Resolved Terahertz Spectroscopy. *Rev. Mod. Phys.* **2011**, *83* (2), 543–586. https://doi.org/10.1103/RevModPhys.83.543.

(31) Pattengale, B.; Neu, J.; Ostresh, S.; Hu, G.; Spies, J. A.; Okabe, R.; Brudvig, G. W.; Schmuttenmaer, C. A. Metal–Organic Framework Photoconductivity via Time-Resolved Terahertz Spectroscopy. *J. Am. Chem. Soc.* **2019**, *141* (25), 9793–9797. https://doi.org/10.1021/jacs.9b04338.

(32) Capobianco, M. D.; Pattengale, B.; Neu, J.; Schmuttenmaer, C. A. Single Copper Atoms Enhance Photoconductivity in G-C_3N_4. *J. Phys. Chem. Lett.* **2020**, *11* (20), 8873–8879. https://doi.org/10.1021/acs.jpclett.0c02756.

(33) Capobianco, M. D.; Younan, S. M.; Tayvah, U.; Pattengale, B.; Neu, J.; Gu, J.; Brudvig, G. W. Terahertz Conductivity of Semiconducting 2H and Metallic 1T Phases of Molybdenum Disulfide. *J. Phys. Chem. Lett.* **2022**, *13* (35), 8319–8326. https://doi.org/10.1021/acs.jpclett.2c02283.

(34) Prechtel, L.; Song, L.; Schuh, D.; Ajayan, P.; Wegscheider, W.; Holleitner, A. W. Time-Resolved Ultrafast Photocurrents and Terahertz Generation in Freely Suspended Graphene. *Nat. Commun.* **2012**, *3* (1), 646. https://doi.org/10.1038/ncomms1656.

(35) Docherty, C. J.; Parkinson, P.; Joyce, H. J.; Chiu, M.-H.; Chen, C.-H.; Lee, M.-Y.; Li, L.-J.; Herz, L. M.; Johnston, M. B. Ultrafast Transient Terahertz Conductivity of Monolayer MoS_2 and WSe_2 Grown by Chemical Vapor Deposition. *ACS Nano* **2014**, *8* (11), 11147–11153. https://doi.org/10.1021/nn5034746.

(36) Zhang, H.; Yu, A. Photophysics and Photocatalysis of Carbon Nitride Synthesized at Different Temperatures. *J. Phys. Chem. C* **2014**, *118* (22), 11628–11635. https://doi.org/10.1021/jp503477x.

(37) Merschjann, C.; Tyborski, T.; Orthmann, S.; Yang, F.; Schwarzburg, K.; Lublow, M.; Lux-Steiner, M.-Ch.; Schedel-Niedrig, Th. Photophysics of Polymeric Carbon Nitride: An Optical Quasimonomer. *Phys. Rev. B* **2013**, *87* (20), 205204. https://doi.org/10.1103/PhysRevB.87.205204.

(38) Godin, R.; Wang, Y.; Zwijnenburg, M. A.; Tang, J.; Durrant, J. R. Time-Resolved Spectroscopic Investigation of Charge Trapping in Carbon Nitrides Photocatalysts for Hydrogen Generation. *J. Am. Chem. Soc.* **2017**, *139* (14), 5216–5224. https://doi.org/10.1021/jacs.7b01547.

(39) Tayvah, U.; Spies, J. A.; Neu, J.; Schmuttenmaer, C. A. Nelly: A User-Friendly and Open-Source Implementation of Tree-Based Complex Refractive Index Analysis for Terahertz Spectroscopy. *Anal. Chem.* **2021**, *93* (32), 11243–11250. https://doi.org/10.1021/acs.analchem.1c02132.

(40) Shang, B.; Zhao, F.; Choi, C.; Jia, X.; Pauly, M.; Wu, Y.; Tao, Z.; Zhong, Y.; Harmon, N.; Maggard, P. A.; Lian, T.; Hazari, N.; Wang, H. Monolayer Molecular Functionalization Enabled by Acid–Base Interaction for High-Performance Photochemical CO_2 Reduction. *ACS Energy Lett.* **2022**, *7* (7), 2265–2272. https://doi.org/10.1021/acsenergylett.2c01147.

(41) Thurston, J. H.; Hunter, N. M.; Wayment, L. J.; Cornell, K. A. Urea-Derived Graphitic Carbon Nitride (u-g-C_3N_4) Films with Highly Enhanced Antimicrobial and Sporicidal Activity. *J. Colloid Interface Sci.* **2017**, *505*, 910–918. https://doi.org/10.1016/j.jcis.2017.06.089.

(42) Lazauskas, A.; Baltrusaitis, J.; Puodžiukynas, L.; Andrulevičius, M.; Bagdžiūnas, G.; Volyniuk, D.; Meškinis, Š.; Niaura, G.; Tamulevičius, T.; Jankauskaitė, V. Characterization of Urea Derived Polymeric Carbon Nitride and Resultant Thermally Vacuum Deposited Amorphous Thin Films: Structural, Chemical and Photophysical Properties. *Carbon* **2016**, *107*, 415–425. https://doi.org/10.1016/j.carbon.2016.06.019.

(43) Chen, Y.; Qu, Y.; Xu, P.; Zhou, X.; Sun, J. Insight into the Influence of Donor-Acceptor System on Graphitic Carbon Nitride Nanosheets for Transport of Photoinduced Charge Carriers and Photocatalytic H_2 Generation. *J. Colloid Interface Sci.* **2021**, *601*, 326–337. https://doi.org/10.1016/j.jcis.2021.05.145.

(44) Zhang, G.; Li, G.; Lan, Z.-A.; Lin, L.; Savateev, A.; Heil, T.; Zafeiratos, S.; Wang, X.; Antonietti, M. Optimizing Optical Absorption, Exciton Dissociation, and Charge Transfer of a Polymeric Carbon Nitride with Ultrahigh Solar Hydrogen Production Activity. *Angew. Chem. Int. Ed.* **2017**, *56* (43), 13445–13449. https://doi.org/10.1002/anie.201706870.

(45) Choudhury, B.; Paul, K. K.; Sanyal, D.; Hazarika, A.; Giri, P. K. Evolution of Nitrogen-Related Defects in Graphitic Carbon Nitride Nanosheets Probed by Positron Annihilation and Photoluminescence Spectroscopy. *J. Phys. Chem. C* **2018**, *122* (16), 9209–9219. https://doi.org/10.1021/acs.jpcc.8b01388.

(46) Yuan, Y.; Zhang, L.; Xing, J.; Utama, M. I. B.; Lu, X.; Du, K.; Li, Y.; Hu, X.; Wang, S.; Genç, A.; Dunin-Borkowski, R.; Arbiol, J.; Xiong, Q. High-Yield Synthesis and Optical Properties of g-C_3N_4. *Nanoscale* **2015**, *7* (29), 12343–12350. https://doi.org/10.1039/C5NR02905H.

(47) Bayan, S.; Midya, A.; Gogurla, N.; Singha, A.; Ray, S. K. Origin of Modified Luminescence Response in Reduced Graphitic Carbon Nitride Nanosheets. *J. Phys. Chem. C* **2017**, *121* (35), 19383–19391. https://doi.org/10.1021/acs.jpcc.7b06587.

(48) Wang, Y.; Townsend, P. D. Common Mistakes in Luminescence Analysis. *J. Phys. Conf. Ser.* **2012**, *398*, 012003. https://doi.org/10.1088/1742-6596/398/1/012003.

(49) Spies, J. A.; Hilibrand, M. J.; Neu, J.; Ostresh, S.; Swierk, J. R.; Schmuttenmaer, C. A. Suspensions of Semiconducting Nanoparticles in Nafion for Transient Spectroscopy and Terahertz Photoconductivity Measurements. *Anal. Chem.* **2020**, *92* (6), 4187–4192. https://doi.org/10.1021/acs.analchem.9b05723.

(50) Smith, N. Classical Generalization of the Drude Formula for the Optical Conductivity. *Phys. Rev. B* **2001**, *64* (15), 155106. https://doi.org/10.1103/PhysRevB.64.155106.

(51) Cocker, T. L.; Baillie, D.; Buruma, M.; Titova, L. V.; Sydora, R. D.; Marsiglio, F.; Hegmann, F. A. Microscopic Origin of the Drude-Smith Model. *Phys. Rev. B* **2017**, *96* (20), 205439. https://doi.org/10.1103/PhysRevB.96.205439.

TOC GRAPHIC

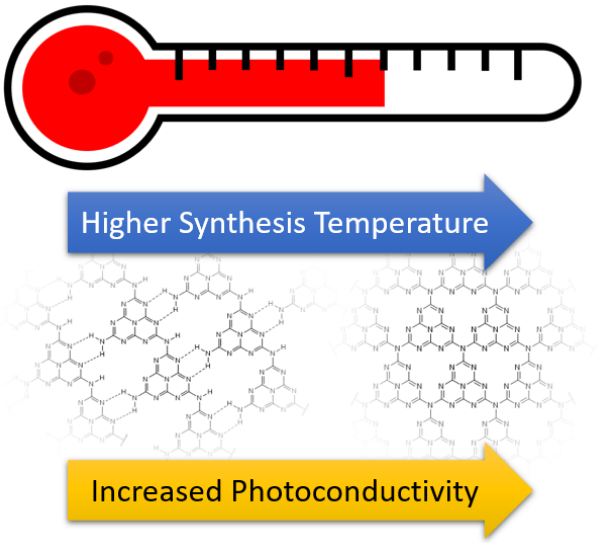
Higher Synthesis Temperature
Increased Photoconductivity